Research article

CO$_2$ conversion in a dielectric barrier discharge plasma by argon dilution over MgO/HKUST-1 catalyst using response surface methodology

Hadi Hatami [a], Mohammadreza Khani [a,*], Seyed Ali Razavi Rad [a], Babak Shokri [a,b]

[a] *Laser and Plasma Research Institute, Shahid Beheshti University, Tehran, Iran*
[b] *Department of Physics, Shahid Beheshti University, Tehran, Iran*

A B S T R A C T

Metal-organic frameworks (MOFs) as carbon dioxide adsorption in combination with metal oxides have shown catalyst application in CO$_2$ conversion. Herein, the MgO/HKUST-1 catalyst is synthesized to direct conversion of CO$_2$ upon dilution by argon in a cylindrical dielectric barrier discharge (DBD) reactor. A water-cooling circulation adjusts the reactor temperature, and aluminum powder is used as a high-voltage electrode. The effect of the discharge power, feed flow rate, CO$_2$ fraction, and their interaction in plasma and plasma catalyst method on CO$_2$ conversion (R$_1$), effective CO$_2$ conversion (R$_2$), and energy efficiency (R$_3$) is evaluated by central composite design (CCD) based on response surface methodology. The Analysis of Variance (ANOVA) results demonstrate that the quadratic regression model describes CO$_2$ conversion and effective CO$_2$ conversion, and the reduced cubic model describes energy efficiency. The results indicate that the method (plasma, plasma catalyst) and discharge power on R$_1$ and R$_2$ have a considerable effect. Also, the method and CO$_2$ fraction on R$_3$ have the greatest impact, respectively. In the plasma and plasma catalyst method maximum CO$_2$ conversion is 12.3% and 20.5% at a feed flow rate of 80 ml/min, CO$_2$ fraction of 50%, and discharge power of 74 W.

1. Introduction

Greenhouse gases, especially carbon dioxide, are the most important cause of global warming [1]. With the beginning of the Industrial Revolution, the use of fossil fuels has increased dramatically and led to greenhouse gas production. The share of carbon dioxide in the production of greenhouse gases is extensively higher than other gases such as methane, nitrous oxide, and fluorinated gases [2, 3]. According to Our World in Data, 6 billion tonnes of CO$_2$, in 1950 was emitted. In 1990, this amount had quadrupled to 22 billion tonnes. Emissions have continued to increase sharply, reaching over 34 billion tonnes per year [4]. These emissions cause increasing global temperature, and researchers are estimated it to be increasing at 0.2 °C per decade [5].

There are different methods to reduce CO$_2$ emissions, among these methods, carbon capture and storage (CCS) and carbon capture and utilization (CCU), have been given more attention [6]. Unlike CCS, the long-term safety of CO$_2$ storage can be ensured using CCU [7], where CO$_2$ is used in some value-added products such as syngas [8], methanol [9], ethanol [10], acetic acid [11], and formic acid [12]. The direct conversion of CO$_2$ to CO according to the following equation (R1) is one of the most promising possible ways for CCU

---

* Corresponding author.
E-mail address: khanimohammadreza@ymail.com (M. Khani).

because CO is an essential chemical feedstock for the synthesis of a wide range of products [13–15].

$$CO_2 \rightarrow CO + \frac{1}{2}O_2 \Delta H = 279.8 \; kJ \Big/ mol \tag{R1}$$

Due to Gibbs free energy of formation of CO2 ($\Delta G = -394$ kJ/mol) and high energy bond C=O (783 kJ/mol), CO_2 is a highly stable molecule, so decomposition of CO_2 requires substantial energy [16]. Due to requirements for high temperatures (3000–3500 K) to splitting CO_2 in traditional methods such as pyrolysis, it not only consumes a lot of energy but also has low conversion and energy efficiency [13,17]. In addition, thermal methods in catalysis are also not effective method because of high energy consumption and deactivation of the catalyst due to the formation of coke on catalyst [18]. Because of the unproductive thermal methods, several promising approaches have been progressively developed such as electrochemical conversion [19], solar thermochemical conversion [20], photochemical conversion [21], biochemical conversion [22], photocatalysis conversion [23], and plasma conversion [16]. Different plasma configurations like corona discharges [24], gliding arc discharges [25], microwave discharges [26], and dielectric barrier discharges (DBDs) have been used for this purpose [27]. Among various plasma configurations, DBDs have some benefits such as high-energy electron (1–10 ev), the capability to initiate endothermic chemical reactions at ambient conditions, and uniform distribution of discharge [16]. In order to increase conversion, energy efficiency, selectivity, and yield, combined plasma with catalysts are used. The addition of a catalyst to a plasma reactor can lead to synergy effects between the plasma and the catalyst [28]. Peiyu Wu et al. [29] used aluminum as the inner electrode because it has moderate thermal and electrical conductivity, and adding $MgTiO_3$ as a catalyst had maximum CO_2 conversion. Na Lu et al. [30] showed that a water-cooling circulation system increased conversion, due to reduced recombination reaction in a DBD reactor with KuCN/AO catalyst. Na Lu et al. [31] showed that the use of compact conductive powder as a high-voltage electrode instead of a rod electrode in a DBD reactor caused an increase in conversion, yield, and energy efficiency. Some research indicates a dilution of CO_2 with argon, increases CO_2 conversion [32,33]. Ramakers et al. [32] investigated raising CO_2 conversion and reduced breakdown voltage by the addition of Ar and He in a DBD.

Among different catalysts, metal-organic frameworks (MOFs) have gained interest because they exhibit high specific surface area, high porosity, and tunable functional structure [34]. MOFs are composed of metal nodes and organic ligands through coordination bonds [35]. HKUST-1 (also known as $Cu_3(BTC)_2$) as a catalyst has outstanding CO_2 adsorption capacity, high surface area, and chemical stability [36]. The combination of metal oxides with MOFs has shown synergistic effects in various applications such as catalysts and sensing [37]. Research has shown that MgO as a promoter can reduce the reaction temperature and also improve the CO_2 adsorption capacity at low temperatures by increasing the Lewis base sites [38,39]. Therefore, the combination of MgO/HKUST-1 can be effective in the field of plasma catalysts to enhance the CO_2 conversion rate.

In order to study the interactions between various parameters, DoE is an effective design tool that is versatile for various complex processes. Based on statistical and mathematical techniques, Response surface methodology (RMS) optimizes the performance of complex systems based on non-linear relationships between multiple inputs and output variables [40].

In this study, the efficacy of dilution by argon on CO_2 dissociation in a DBD plasma system with a high-voltage electrode made of aluminum powder and a water-cooling circulation system to adjust the reactor temperature in the presence of a MgO/HKUST-1 catalyst, for the first time, has been investigated. The catalyst is characterized by field emission scanning electron microscopy (FE-SEM), energy dispersive X-ray spectroscopy (EDS), X-ray diffraction (XRD), and N_2 adsorption-desorption (BET). The effect of three process parameters including the discharge power, feed flow rate, CO_2 fraction, and their interaction on CO_2 conversion and energy efficiency using the RMS based on central composite design (CCD) has been investigated.

2. Experimental

2.1. Catalyst preparation

Porous HKUST-1 is synthesized by hydrothermal method. Solution A is 2.35 g $Cu(NO_3)_2.6H_2O$ which is dissolved in 15 ml deionized water and solution B is 1 g of benzene-1,3,5-tricarboxylic acid is dissolved in 30 ml ethanol and N.N–dimethylformamide. Solution A and B are mixed, and it is added to a teflon-lined stainless steel autoclave. The solution is placed in the oven at 100 °C for 10 h, then, it is cooled to room temperature naturally and washed with deionized water and ethanol. To synthesize MgO/HKUST-1 the hydrothermal method has been used. Solution A is prepared to synthesize by dispersing about 0.32 g of MgO nanoparticles with 0.96 g of Cu $(NO_3)_2.6H_2O$ in 40 ml of deionized water for 12 h. Solution B is prepared by adding about 0.64 g of benzene-1,3,5-tricarboxylic acid in 40 ml of ethanol and deionized water (DI) (20 ml ethanol, 20 ml DI), and the solution is stirred. Solution A and Solution B were mixed thoroughly, and is transferred to a Teflon-lined stainless steel autoclave and placed in an oven at 110 °C for 18 h. After that, the autoclave is cooled to room temperature, and the solution is washed several times with deionized water and ethanol and dried to obtain the final catalyst.

2.2. Catalyst characterization

Field emission scanning electron microscopy (FE-SEM, MIRA3, TESCAN) equipped with an energy dispersive x-ray spectroscopy (EDS) is used to characterize local morphologies and each chemical element of the catalyst. X-ray diffraction analysis (XRD, STOE-IPDS II) is done to identify the crystallinity of the samples. The scan range of 2θ angle is 1–80 with a CuKα radiation source. In addition, the applied voltage and current are 40 kV and 40 mA, respectively. N_2 adsorption-desorption (BET) (Micromeritics) analysis determines

the specific surface area, pore size distributions, and pore volume of the catalyst by a physical adsorption analyzer.

2.3. Experimental setup

CO_2 conversion is performed in a cylindrical DBD reactor at atmospheric pressure. Fig. 1 (a) shows the schematic diagram of the system setup. Fig. 1 (b) shows the schematic diagram of the cylindrical DBD reactor, which includes two quartz tubes with outer diameters of 28 mm and 21 mm, and the thickness of each is 1.5 mm. A water-cooling circulation system on the exterior of the outer quartz tube has been used to control the reaction temperature, which is made of plexiglass with a diameter of 10 cm. Inside the inner quartz tube, aluminum powder is used as the high-voltage electrode, whereas stainless steel mesh is wrapped around the outer quartz as the ground electrode. The discharge length is 10 cm, and the 2 mm gap is filled with a catalyst; to keep the catalyst fixed in the desired place inside the plasma area, both sides are held with glass wool. DBD is connected to an AC high-voltage generator with a peak-to-peak voltage of 3–12 kV and 32 kHz frequency. The applied voltage is measured by a high-voltage probe (Tektronix P6015A). The plasma discharge power is obtained using the Q-V Lissajour method [41]. To measure the accumulated charge in the discharge process, the capacitor (3.3 nF) voltage is measured by a low-voltage probe (Tektronix P2220). All electrical signals are recorded by a Tekronix (DPO 3012) two-channel oscilloscope.

In this experiment, high-purity CO_2 gas and Ar gas as feed gas with a flow rate of 80–140 ml/min are used, with CO_2 fractions 100, 75, and 50%, and a Mass flowmeter (MFC; ALICAT MC) is used to control the gas flow. The gas products are analyzed by an electrochemical gas analyzer (PTM600-6).

The discharge power is calculated by a Lissajous curve approach introduced by Manley in 1943 [42]. Discharge power obtained based on equation (1):
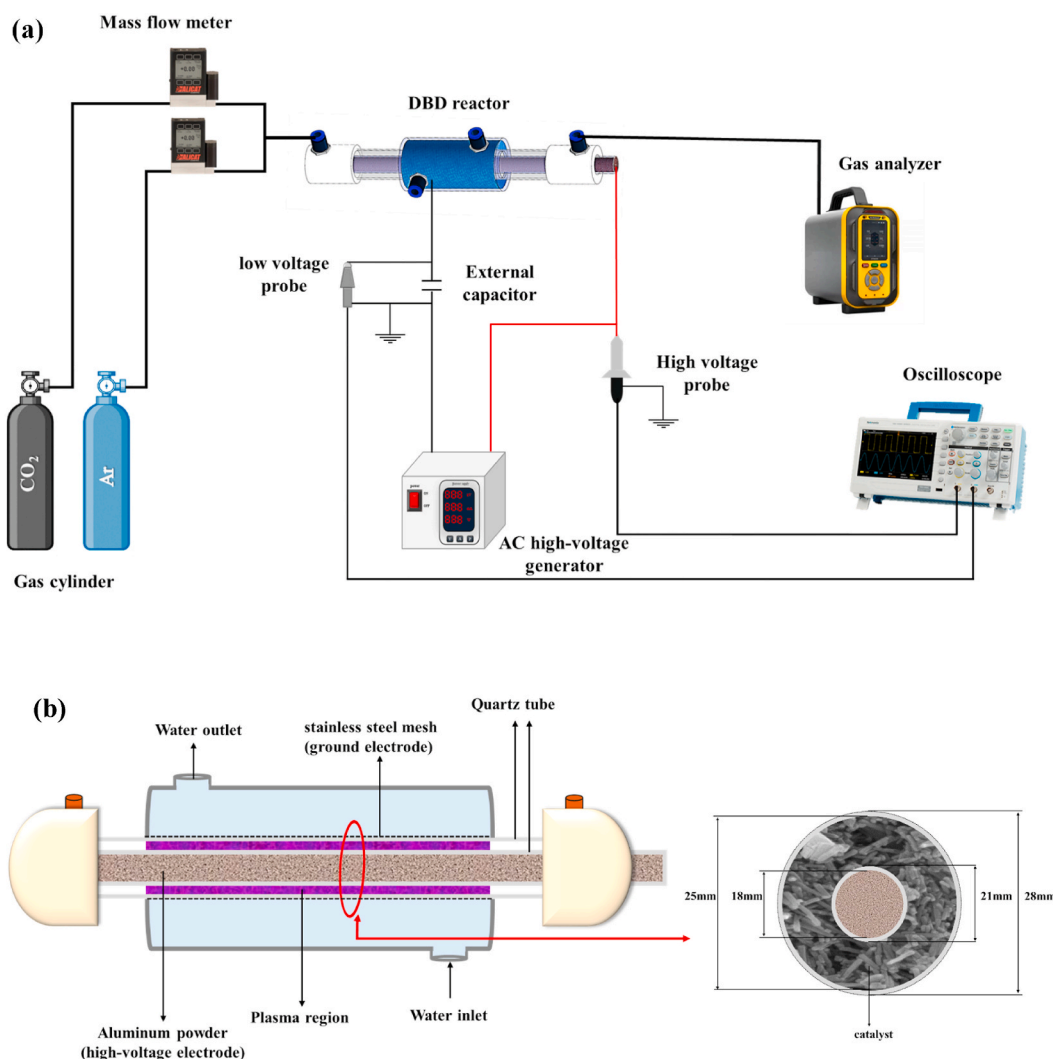

Fig. 1. (a) schematic diagram of the system setup, (b) schematic diagram of the cylindrical DBD reactor.

$$P = f.E = f. \int_T U(t).I(t)dt = f. \int_T U(t).\frac{dQ(t)}{dt} dt = f.C \int_T U(t).dV_C(t) \tag{1}$$

U(t) and I(t) are the applied voltage and the discharge current, f is the constant frequency (32 kHz), and C is an external capacitor, which $V_C(t)$ is the voltage across the capacitor.

The conversion rate of CO_2 (C_{CO_2} based on equation (2)), the effective CO_2 conversion ($C_{CO_2\ eff}$ based on equation (3)), the specific energy input (SEI based on equation (4)), and the energy efficiency (η based on equation (5)) are determined as follows:

$$C_{CO_2}(\%) = \frac{C_{CO_2}\ input\left(\frac{ml}{min}\right) - C_{CO_2}\ output\left(\frac{ml}{min}\right)}{C_{CO_2}\ input\left(\frac{ml}{min}\right)} * 100 \tag{2}$$

$$C_{CO_2\ eff}(\%) = C_{CO_2}(\%) \frac{C_{CO_2}\ input\left(\frac{ml}{min}\right)}{C_{CO_2}\ input\left(\frac{ml}{min}\right) + Ar\ input\left(\frac{ml}{min}\right)} * 100 \tag{3}$$

$$SEI\left(\frac{kj}{l}\right) = \frac{60 * Discharge\ power\ (W)}{Total\ feed\ flow\ rate\left(\frac{ml}{min}\right)} \tag{4}$$

$$\eta = \frac{\Delta H\left(\frac{kJ}{mol}\right) * C_{CO_2\ eff}(\%)}{22.4 * SEI\left(\frac{kJ}{l}\right)} \tag{5}$$

Where $\Delta H = 283 \frac{kJ}{mol}$ is the reaction enthalpy of CO_2 conversion.

2.4. Response surface process

This study investigates a three-level, four-factor CCD based on RMS to identify the effect of each independent parameter and the interaction between these different parameters on the CO_2 conversion process. Based on the papers [32,33,43], the effective parameters on the CO_2 conversion are discharge power (A), feed flow rate (B), and CO_2 fraction (C), and another parameter is the method (D), which is a categoric factor in two levels including plasma, and plasma catalyst (MgO/HKUST-1 catalyst), so these parameters are chosen as input for the design, while the CO_2 conversion (R_1), the effective CO_2 conversion (R_2), and energy efficiency (R_3) are employed as responses. Each factor includes three different levels with coded −1(low), 0 (center), and 1 (high), as shown in Table 1.

In CCD design, the quadratic regression model describes the interrelationship between different independent factors and output responses for CO_2 conversion and effective CO_2 conversion, and the reduced cubic model describes energy efficiency. The analysis of variance (ANOVA) describes the adequacy and fit of the model. The F-test and the adequacy of measurement, such as the coefficient of determination R^2, adjusted R^2, and predicted R^2, can identify the statistical significance of the models and each term. In a well-developed model, the difference between the predicted R^2 and adjusted R^2 should be less than 0.2 [44].

3. Results and discussion

3.1. Catalyst characterization

Fig. 2(a–c) shows surface morphology and microstructure patterns of HKUST-1, MgO, and MgO/HKUST-1, which are observed by the FE-SEM. As expected HKUST-1 has an octahedral structure (Fig. 2 (a)) [45–47], and magnesium oxide has a hexagonal plate morphology (Fig. 2 (b)). Combining inorganic materials with metal oxides creates a close morphology like metal oxides [47]. In this study, the synthesis of MgO with HKUST-1, as is clear in Fig. 2 (c) creates a nanoplate morphology, which is almost like MgO morphology. Meanwhile, the EDS reveals that C, O, Mg, and Cu with weight content of 18.1, 37.82, 14.13, and 29.95% are quantified,

Table 1
Independent variables and their Levels and ranges used in CCD.

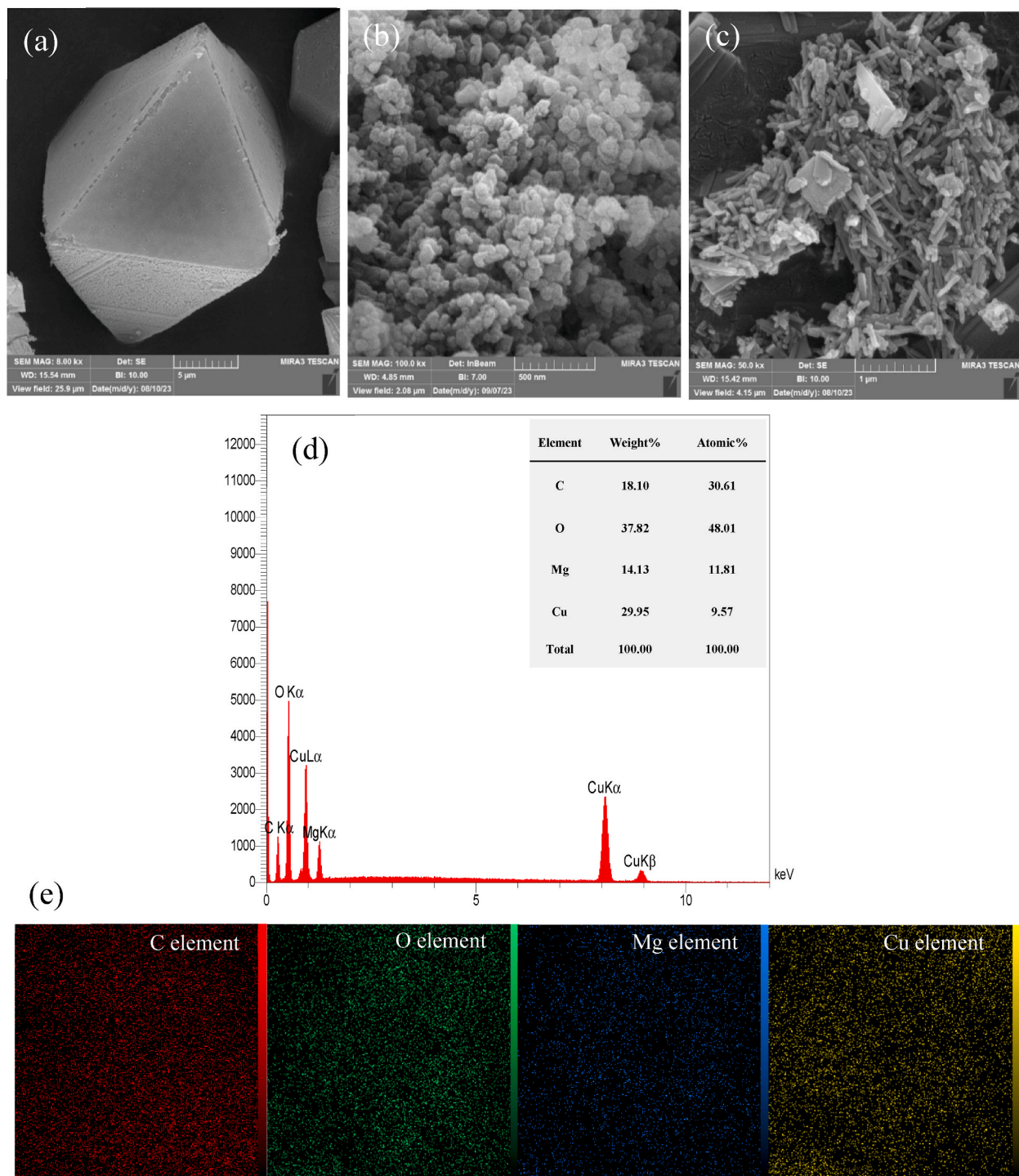| Independent variables	Coded factors	Levels and ranges		
		−1 (Low)	0 (Center)	1 (High)
Discharge power (W)	A	30	52	74
feed flow rate (ml/min)	B	80	110	140
CO_2 fraction (%)	C	50	75	100

Fig. 2. (a) FE-SEM image of HKUST-1, (b) FE-SEM image of MgO, (c) FE-SEM image of MgO/HKUST-1 (d) EDS for MgO/HKUST-1, (e) and EDS element maping images of C, O, Mg, and Cu.

respectively (Fig. 2 (d)). In this analysis, an Mg peak confirms that the MgO/HKUST-1 has been successfully synthesized. Moreover, elemental mapping in Fig. 2 (e) reveals that the C, O, Mg, and Cu elements are uniformly distributed throughout the surface.

Fig. 3 indicates an XRD pattern to identify the crystalline structure of the HKUST-1, MgO, and MgO/HKUST-1. The XRD pattern shows peaks at $2\theta = 6.7°$, $9.4°$, $11°$, $13.4°$, $19°$, $26°$, and $29.4°$, which are defined as (200), (220), (222), (400), (440), (731), and (751) crystal plane of the HKUST-1 [45,48]. In addition, characteristic peaks ascribe to MgO at $2\theta = 36.4°$, $42.9°$, and $61.4°$ that correspond
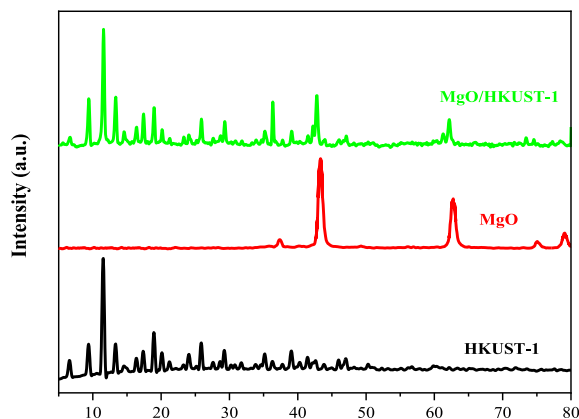
Fig. 3. XRD patterns of HKUST-1, MgO, MgO/HKUST-1.

to (111), (200), and (220) crystal plane [47,49].

The specific surface areas and the average pore volumes and pore diameters of HKUST-1, MgO, and MgO/HKUST-1 are measured by the BET method and the Barrett, Joyner, and Halenda (BJH method), as shown in Fig. 4(a–c). The results in Table 2 indicate that the samples have mesoporous structure (type IV isotherms) and the specific surface areas of MgO with the HKUST-1 introduction are increased.

Fig. 4. N$_2$ adsorption–desorption isotherms and BJH plots (inset) (a) HKUST-1, (b) MgO, (c) MgO/HKUST-1.

Table 2
specific surface areas, pore volumes, and pour diameters of samples.
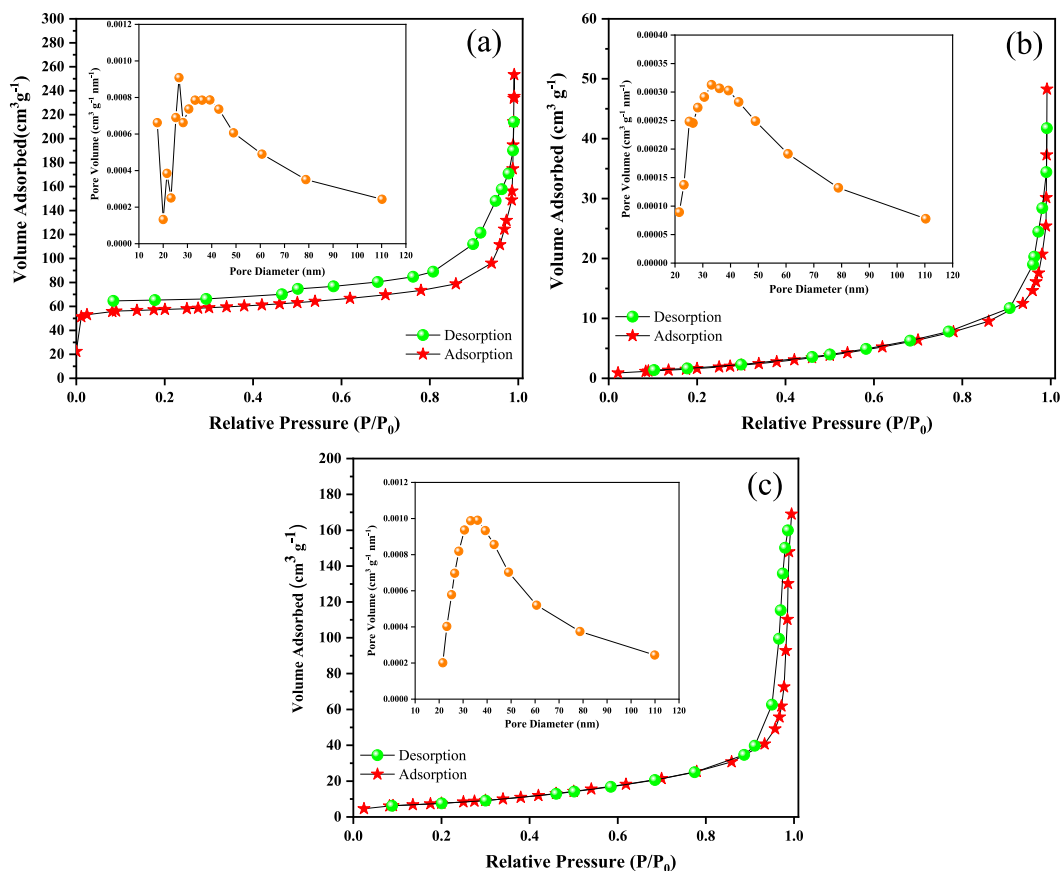
Samples	S_{BET} (m^2/g)	P_{vol} (cm^3/g)	P_{diam} (Å)
HKUST-1	188.6254	0.075	59.96
MgO	6.9191	0.017	48.31
MgO/HKUST-1	28.6801	0.055	52.12

Table 3
Experimental design and the results of the CCD.

Run order	Independent variables				Responses		
	A: Discharge power (W)	B: Feed flow rate	C:CO$_2$ fraction	D: Method	R$_1$: Conversion (%)	R$_2$: Effective conversion (%)	R$_3$: Energy efficiency (%)
1	52	80	75	plasma catalyst	16.8	12.6	4.1
2	74	110	75	plasma	10.5	7.9	2.5
3	30	80	100	plasma catalyst	11.5	11.5	6.5
4	52	140	75	plasma	5.3	3.975	2.2
5	30	140	100	plasma catalyst	9.5	9.5	9.3
6[b]	52	110	75	plasma catalyst	16.1	12.1	5.4
7	30	140	50	plasma catalyst	11.5	5.7	5.6
8	74	110	75	plasma catalyst	17.1	12.8	4
9	30	80	50	plasma catalyst	13.5	6.7	3.8
10[a]	52	110	75	plasma	7.8	5.8	2.6
11	74	80	100	plasma catalyst	17.3	17.3	3.9
12	52	110	50	plasma	8.9	4.4	2
13[a]	52	110	75	plasma	7.9	5.9	2.6
14[b]	52	110	75	plasma catalyst	16	12	5.3
15	74	80	50	plasma catalyst	20.5	10.2	2.3
16	74	140	50	plasma	9.9	4.9	2
17	52	110	50	plasma catalyst	17	8.5	3.8
18	30	110	75	plasma	5.2	3.9	3
19	30	140	100	plasma	2.8	2.8	2.7
20	74	140	100	plasma catalyst	14.5	14.5	5.8
21	74	140	100	plasma	6.9	6.9	2.7
22	52	140	75	plasma catalyst	14.2	10.6	6
23	52	80	75	plasma	8.8	6.6	2.1
24	74	80	100	plasma	8.5	8.5	1.9
25	74	80	50	plasma	12.3	6.1	1.4
26	30	80	100	plasma	4.7	4.7	2.6
27	52	110	100	plasma catalyst	15	15	6.7
28	30	140	50	plasma	4.5	2.2	2.2
29	74	140	50	plasma catalyst	17	8.5	3.4
30	30	110	75	plasma catalyst	12.2	9.15	7
31[b]	52	110	75	plasma catalyst	16.2	12.1	5.4
32	52	110	100	plasma	6.8	6.8	3
33	30	80	50	plasma	6.5	3.2	1.8
34[a]	52	110	75	plasma	8.5	6.4	2.8

[a] Replicated experimental runs in plasma method.
[b] Replicated experimental runs in plasma catalyst method.

3.2. DoE analysis

3.2.1. Regression model

In this study, 34 experiments have been done on CO_2 conversion for the CCD model, including three replicated experimental runs (No. 10, 13, and 34 for the plasma method; No. 6, 14, and 31 for the plasma catalyst method). The design of experiments and responses are summarized in Table 3. The relationship between input factors and responses is described by the quadratic models and the reduced cubic model as follows:

R_1: CO_2 conversion (%):

$$11.99 + 2.63A\text{-}1.22B\text{-}1.2C + 3.83D\text{-}0.15AB\text{-}0.3125AC + 0.19AD + 0.1BC\text{-}0.075BD + 0.035CD\text{-}0.66A^2\text{-}0.64B^2 + 0.01\,C^2 \tag{6}$$

R_2: Effective CO_2 conversion:

$$9 + 1.91A\text{-}0.8912B + 1.84C + 2.87D\text{-}0.0906AB + 0.4281AC + 0.1625AD\text{-}0.2094BC\text{-}0.0587BD$$
$$+ 0.97CD\text{-}0.5202A^2\text{-}0.5015B^2\text{-}0.2702C^2 \tag{7}$$

R_3: Energy efficiency (%):

$$4.01\text{-}0.7279A + 0.5771B + 0.8379C + 1.36D\text{-}0.0464AB\text{-}0.1536AC\text{-}0.5479AD + 0.1089BC + 0.3771BD + 0.4879CD$$
$$+ 0.1278A^2\text{-}0.3972B^2\text{-}0.1222C^2\text{-}0.1589ABD\text{-}0.1411ACD + 0.1214BCD + 0.0067A^2D + 0.0817\,B^2D + 0.0067\,C^2D \tag{8}$$

The ANOVA to determine the significance and adequacy of the regression models is exhibited in Table 4, Table 5, and Table 6. The ANOVA results confirm that the regression models are statistically significant due to F-values being higher than the critical value in this study (2.25 in quadratic models and 2.4 in reduced cubic model) [44]. Moreover, results illustrate that the model is significant and adequate because at a confidence level higher than 95%, the p-value for the responses R_1, R_2, and R_3 is lower than 0.05 (<0.0001 for R_1, R_2, and R_3). The lack of fit for responses is insignificant(0.1151, 0.0687, and 0.098, respectively). The regression correction coefficients (R^2) for the CO_2 conversion, the effective CO_2 conversion, and energy efficiency are 0.9935, 0.9926, and 0.9969 that demonstrate the experimental data and regression model are fitted. The difference between predicted R^2 and adjusted R^2 for R_1, R_2, and R_3 is less than 0.2, indicating the models' stability and validity.

The adequate precision measures the signal-to-noise ratio (a ratio greater than four is desirable), which is 57.39, 55.79, and 64.99 for the CO_2 conversion, the effective CO_2 conversion, and energy efficiency, which illustrate adequate intensities of the signals. In this study, the coefficient of variations (C.V.) is less than 10% (4.29, 5.09 for R_1, R_2, and 4.27 for R_3), which shows the reliability and reproducibility of the models.

3.2.2. Effect of plasma process parameters on CO_2 conversion and effective CO_2 conversion

Fig. 5 indicates CO_2 conversion in the DBD plasma reactor in the presence of HKUST-1 and MgO/HKUST-1 catalyst at a feed flow rate of 50 ml/min. CO_2 conversion is increased in both case catalysts by increasing SEI, whereas energy efficiency is decreased. These results show MgO/HKUST-1 has better performance in conversion and energy efficiency. At SEI of 88.8 kJ/L CO_2 conversion with HKUST-1 and MgO/HKUST-1 is 16% and 19.2% respectively.

The specific surface area is directly correlates with CO_2 conversion because increasing the specific surface area creates more active sites for CO_2 adsorption on the catalyst surface and subsequently CO_2 conversion is increased [30]. Although introducing MgO to HKUST-1 reduces the specific surface area (S_{BET}) in comparison with HKUST-1, CO_2 conversion is increased, because of the synergy effect in the catalyst reaction in the MgO/HKUST-1 catalyst [50].

Table 4
The ANOVA results for the quadratic model of the CO_2 conversion.

Source	Sum of squares	Degree of freedom	Mean square	F-value	P-value (Prob > F)	
Model	708.14	13	54.47	234.44	<0.0001	significant
A-power	138.34	1	138.34	595.38	<0.0001	significant
B-flow	29.52	1	29.52	127.07	<0.0001	significant
C–CO_2/Ar	29.04	1	29.04	124.99	<0.0001	significant
D-D	497.82	1	497.82	2142.55	<0.0001	significant
AB	0.36	1	0.36	1.55	0.2276	not significant
AC	1.56	1	1.56	6.72	0.0174	significant
AD	0.722	1	0.722	3.11	0.0932	not significant
BC	0.16	1	0.16	0.6886	0.4164	not significant
BD	0.1125	1	0.1125	0.4842	0.4945	not significant
CD	0.0245	1	0.0245	0.1054	0.7488	not significant
A^2	2.36	1	2.36	10.17	0.0046	significant
B^2	2.19	1	2.19	9.42	0.0061	significant
C^2	0.0006	1	0.0006	0.0027	0.9587	not significant
Residual	4.65	20	0.2324			
Lack of Fit	4.34	16	0.2713	3.54	0.1151	not significant

R^2: 0.9935; Adjusted R^2: 0.9892; Predicted R^2: 0.9806; Adeq Precision:57.3949.

Table 5

The ANOVA results for the quadratic model of the effective CO_2 conversion.

Source	Sum of squares	Degree of freedom	Mean square	*F*-value	*P*-value (Prob > F)	
Model	469.86	13	36.14	205.27	<0.0001	significant
A-power	72.96	1	72.96	414.38	<0.0001	significant
B-flow	15.89	1	15.89	90.22	<0.0001	significant
C–CO_2/Ar	67.34	1	67.34	382.47	<0.0001	significant
D-D	281.03	1	281.03	1596.07	<0.0001	significant
AB	0.1314	1	0.1314	0.7463	0.3979	not significant
AC	2.93	1	2.93	16.66	0.0006	significant
AD	0.5281	1	0.5281	3	0.0987	not significant
BC	0.7014	1	0.7014	3.98	0.0597	not significant
BD	0.069	1	0.069	0.3921	0.5383	not significant
CD	18.82	1	18.82	106.87	<0.0001	significant
A^2	1.45	1	1.45	8.24	0.0095	not significant
B^2	1.35	1	1.35	7.65	0.0119	significant
C^2	0.3913	1	0.3913	2.22	0.1516	not significant
Residual	3.52	20	0.1761			
Lack of Fit	3.35	16	0.2093	4.85	0.0687	not significant

R^2: 0.9926; Adjusted R^2: 0.9877; Predicted R^2: 0.9767; Adeq Precision: 55.7912.

Table 6

The ANOVA results for the reduced cubic model of the energy efficiency.

Source	Sum of Squares	Degree of freedom	Mean Square	F-value	p-value (Prob > F)	
Model	116.15	19	6.11	234.99	<0.0001	significant
A-power	10.6	1	10.6	407.32	<0.0001	significant
B-flow	6.66	1	6.66	256.08	<0.0001	significant
C–CO_2/Ar	14.04	1	14.04	539.73	<0.0001	significant
D-D	20.22	1	20.22	777.17	<0.0001	significant
AB	0.0345	1	0.0345	1.33	0.269	not significant
AC	0.3774	1	0.3774	14.51	0.0019	significant
AD	6	1	6	230.77	<0.0001	significant
BC	0.1898	1	0.1898	7.3	0.0172	significant
BD	2.84	1	2.84	109.35	<0.0001	significant
CD	4.76	1	4.76	182.99	<0.0001	significant
A^2	0.0875	1	0.0875	3.37	0.0879	not significant
B^2	0.8453	1	0.8453	32.49	<0.0001	significant
C^2	0.08	1	0.08	3.07	0.1014	not significant
ABD	0.4041	1	0.4041	15.53	0.0015	significant
ACD	0.3185	1	0.3185	12.24	0.0035	significant
BCD	0.2359	1	0.2359	9.07	0.0093	significant
A^2D	0.0002	1	0.0002	0.0092	0.9248	not significant
B^2D	0.0358	1	0.0358	1.37	0.2606	not significant
C^2D	0.0002	1	0.0002	0.0092	0.9248	not significant
Residual	0.3642	14	0.026			
Lack of Fit	0.3309	10	0.0331	3.97	0.098	not significant

R^2: 0.9969; Adjusted R^2: 0.9926; Predicted R^2:0.9714; Adeq Precision: 64.99.

The ANOVA results illustrate the effect of independent variables and their interaction on CO_2 conversion. In this model, A, B, C, D, AC, A^2, and B^2 are significant parameters for the CO_2 conversion and the effective CO_2 conversion because the p-value of a parameter is below 0.05. Additionally, CD is also a significant parameter in the effective CO_2 conversion. These parameters indicate that the in-dividual parameters are more important. The F-value determines the relative importance of a term. Due to the high F-value, the most significant factor is the method and then discharge power.

The efficacy of each factor and their interaction has been investigated on the CO_2 conversion and the effective CO_2 conversion in terms of three-dimensional response surfaces based on the regression equations (Equations (6) and (7)). Fig. 6 (a) shows the combined effect of input power and feed flow rate on CO_2 conversion at a CO_2 fraction of 75% (center point). Discharge power changed by applying a voltage at a constant frequency; therefore, when the discharge power increased from 30 W to 74 W, the number of micro-discharges and the current intensity in CO_2/Ar increased. This increase causes the generation of more energetic electrons, reaction channels, and reactive species [16]. To effectively use these reactions and species, combining the catalyst with plasma is an efficacious way to activate the catalyst and enhance the plasma reaction [13]. In addition, the increase in flow rate reduces residence time, resulting in a decreased CO_2 conversion because the possibility of CO_2 activation through reaction species and collision with electrons dramatically decreases. In this work, residence time decreases from 10.8 s to 6.2 s when the total flow rate increases from 80 ml/min to 140 ml/min. The highest CO_2 conversion for the plasma catalyst method and the plasma method can be 18.1% and 10.6%, respec-tively, with maximum power (74 W) and minimum feed flow rate (80 ml/min), at the same condition, which shows conversion rate increased by about 71% when the experiments are in the presence of the catalyst. This result indicates that the MgO/HKUST-1 catalyst
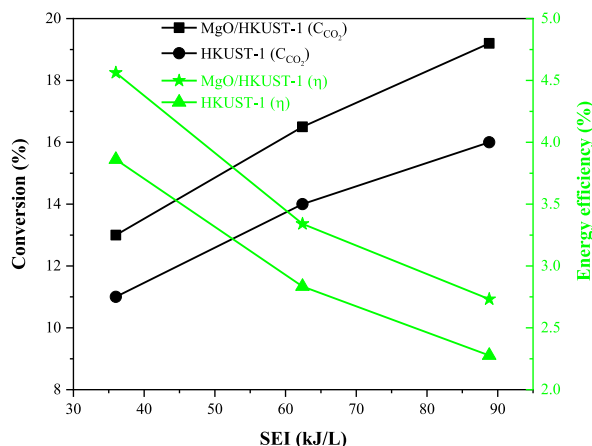
Fig. 5. CO$_2$ conversion and energy efficiency over HKUST-1 and MgO/HKUST-1 in the DBD reactor.
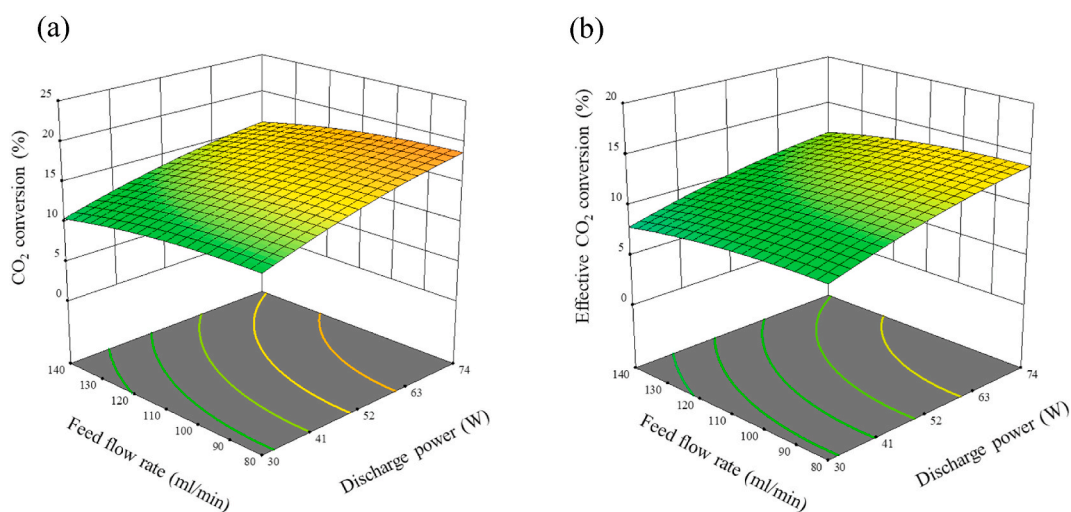

Fig. 6. Interaction between discharge power and feed flow rate on conversion at CO$_2$ fraction of 75%, in plasma catalyst method: (a) CO$_2$ conversion; (b) effective CO$_2$ conversion.

is successfully activated by plasma and increases significantly conversion. Generally, reactive species are reacted with the surface of the catalyst and these species can activate the catalyst, and photon irradiation in plasma can increase catalyst activity. Meanwhile, plasma by change in physiochemical properties (like increasing adsorption at the surface of the catalyst, and higher surface area), work function (due to voltage and current in the plasma region), and creating hot spots by strong microdischarge (which can activate catalyst thermally and modify plasma chemistry) can modify the catalyst. On the other hand, changes in discharge type, increasing electric field, and charge transfer are some of the effects of the catalyst on plasma [13,16,28].

The interaction between HKUST-1 and CO$_2$ is through the Cu^{2+} metallic center. There are two adsorption sites in HKUST-1, the first one through Cu^{2+} on the surface of the catalyst or Cu^{2+} because of structural defects, and another one through the inner framework of the catalyst. In addition, The CO$_2$ physisorption process involves the binding of the CO$_2$ molecule to the Cu^{2+} center of HKUST-1 [51]. Also, the CO$_2$ adsorption on MgO occurs through monodentate and bidentate carbonate species [52].

In the effective CO$_2$ conversion (Fig. 6 (b)), because the amount of CO$_2$ is decreased, these values are 13.9% and 7.8%, respectively. The projected contour plots show the interaction between two terms in the CO$_2$ conversion, and the effective CO$_2$ conversion is insignificant because the gradients at a varied discharge power and gas flow rate are almost the same. The contours are practically parallel, and the high p-value of AB supports this conclusion [53,54].

Fig. 7 (a) illustrates the combined effect of the discharge power and CO$_2$ fraction at a feed flow rate of 110 ml/min (center point) on CO$_2$ conversion. The maximum conversion of CO$_2$ in the plasma catalyst method can be 19.4%, and in the plasma method, 11.5% is achieved at 74 W discharge power and a CO$_2$ fraction of 50%. It is clear that the conversion of CO$_2$ rises with a reduction in CO$_2$ fraction and an increase in Ar fraction, and as expected, when discharge power increases, the CO$_2$ conversion in both cases is increased. The contour lines of discharge power and CO$_2$ fraction show that the interaction between discharge power and CO$_2$ fraction is significant,
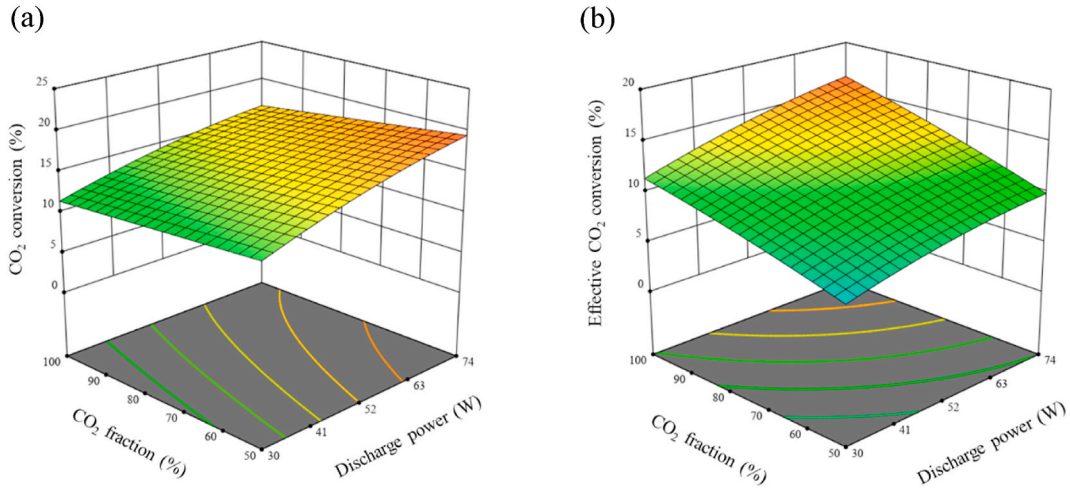
(a)   (b)

Fig. 7. Interaction between discharge power and CO_2 fraction on conversion at feed flow rate of 110 ml/min, in plasma catalyst method: (a) CO_2 conversion; (b) effective CO_2 conversion.

and the p-value also confirms this conclusion. To explain the effect of dilution on conversion, the Lissajous plots are analyzed. Fig. 8 shows the Lissajous plots for pure CO_2 and CO_2 fraction 50%. The Lissagous figures show that in plasma off state, the total capacity of the reactor (C_{cell}) is almost the same because the capacity of the dielectric is equal and the capacity of the gases is slightly different. The lines DA and CB demonstrate plasma off state, and the slope of these lines elucidate C_{cell}. The lines AB and DC show plasma on state, and the slope of these lines demonstrates the effective capacity of the reactor (C_{eff}) [32]. The addition of Ar to CO_2 increases the C_{eff}, which indicates creating more micro-discharge. As can be deduced from the Lissajous figures, U_{min} drops when Ar is added to CO_2, leading to a drop breakdown voltage [32]. The Townsend ionization coefficient (α) is one of the reasons for the reduction of breakdown voltage because α is higher in pure Ar than in pure CO_2 [55]. Therefore, adding Ar to pure carbon dioxide leads to an increase in α and the micro-discharge, which produces more electrons and reactive species per unit discharge length. Since the ionization and excitation of Ar need more electron energy (15.8 eV and 11.5 eV, respectively) compared to CO_2 (13.8 eV and 6.2 eV), most of the plasma energy is used for excitation (R2), electron-induced dissociation (R3), ionization (R4), and the reaction of electron with CO_2^+ (R5) [33]. On the other hand, metastable Ar species (Ar*) usually create new reaction routes to CO_2 dissociation (R6,R7) [56]. Furthermore, the transfer of charge from Ar^+ ions to CO_2 leads to the formation of CO_2^+ ions (R8) [56], which can then undergo dissociative electron-ion recombination (R5), thus significantly contributing to the splitting of CO_2. Consequently, these cases can potentially enhance CO_2 conversion in the presence of Ar, with a higher proportion of Ar resulting in an increased conversion rate. On the other hand, the effective CO_2 conversion has an opposite trend with rising CO_2 fraction compared to CO_2 conversion, as clear in Fig. 7 (b), because there are more CO_2 molecules in the plasma. With the presence of a catalyst, the interaction is higher, so this causes a more effective conversion. The maximum effective CO_2 conversion in the plasma and the plasma catalyst is 16.3% and 8.3% at CO_2 fraction 100% and discharge power 74 W.

$$e^- + CO_2 \rightarrow e^- + CO_2^* \tag{R2}$$

$$e^- + CO_2^* \rightarrow e^- + CO + O \tag{R3}$$

$$e^- + CO_2 \rightarrow 2e^- + CO_2^+ \tag{R4}$$

$$e^- + CO_2^+ \rightarrow CO + O \tag{R5}$$

$$e^- + Ar \rightarrow e^- + Ar^* \tag{R6}$$

$$Ar^* + CO_2 \rightarrow CO + O + Ar \tag{R7}$$

$$Ar^+ + CO_2 \rightarrow Ar + CO_2^+ \tag{R8}$$

The combined effect of feed flow rate, CO_2 fraction, and their interaction on CO_2 conversion and the effective CO_2 conversion at a discharge power 52 W (center point) is plotted in Fig. 9 (a,b). As discussed before, for the plasma and plasma catalyst method, the residence time is decreased by an increase in the flow rate, and the CO_2 conversion and effective amount are decreased. On the other hand, with a decrease in CO_2 fraction, the CO_2 conversion is increased, and the effective CO_2 conversion is decreased. The interaction between these terms is insignificant as the p-value is greater than 0.05 (0.4164 and 0.0597 for R_1 and R_2), and the contour lines are nearly parallel. The maximum CO_2 conversion in plasma and plasma catalyst method is 12.3%, and 20.5% in minimum feed flow rate (80 ml/min) and CO_2 fraction (50%), and the highest discharge power (74 W). In contrast, the maximum effective CO_2 conversion
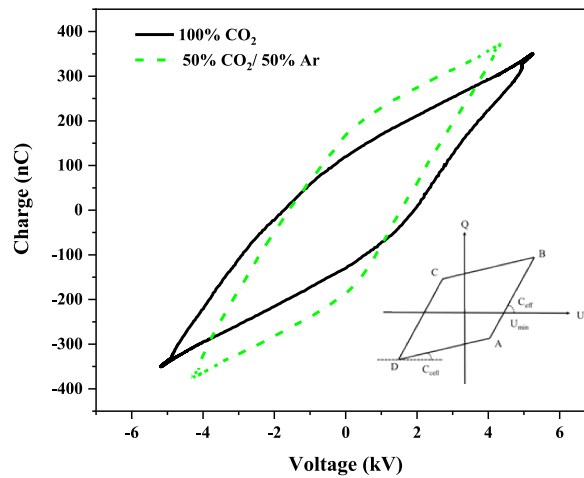
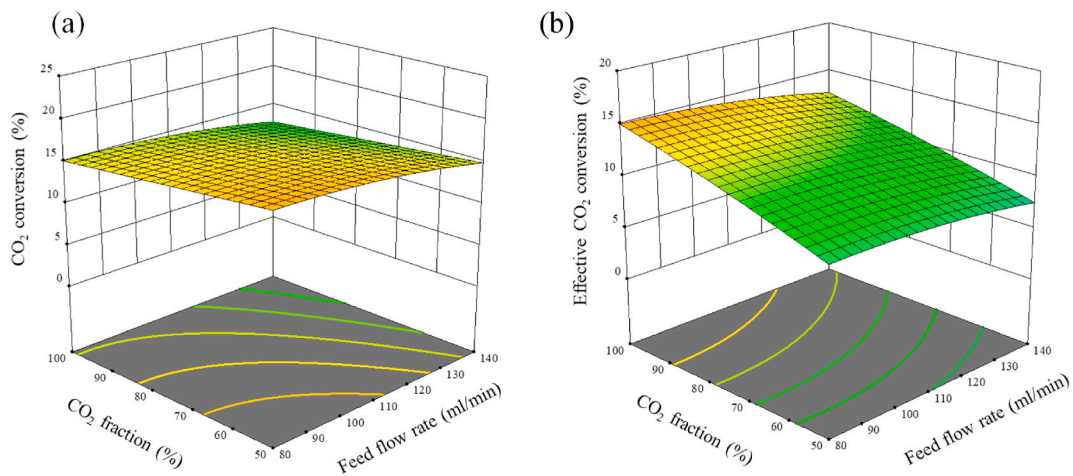**Fig. 8.** Lissajous plots for pure CO_2 and 50% of CO_2, 50% of Ar.

Fig. 9. Interaction between feed flow rate and CO_2 fraction on conversion at discharge power of 52 W, in plasma catalyst method: (a) CO_2 conversion; (b) effective CO_2 conversion.

(8.5%, 17.3%, respectively) is reached with the same condition except for the CO_2 fraction, which must be the highest amount (100% in this case).

3.2.3. Effect of plasma process parameters on energy efficiency

The reduced cubic model expresses the interrelationship between process parameters and energy efficiency and calculates based on Equation (8). A, B, C, D, AC, AD, BC, BD, CD, B^2, ABD, and BCD are significant model terms (p-value <0.05). The method and CO_2 fraction have the most significant efficacy on energy efficiency with F-values 781.48 and 544.82 (shown in Table 6), respectively.

Fig. 10 (a) displays the effect of discharge power and feed flow rate on the energy efficiency in the plasma catalyst method at a CO_2 fraction of 75%. The maximum energy efficiency is 7.5%, which can reach the minimum discharge power of 30 W and the maximum feed flow rate of 140 ml/min and its minimum can be 3.2% at the highest discharge power of 74 W and the lowest feed flow rate of 80 ml/min. In the plasma method, at the same condition, energy efficiency is 2.6% and 1.8%, respectively. Meanwhile, The interaction between these two process parameters in energy efficiency is insignificant (p-value is 0.269). It is worth mentioning that there is a tradeoff between conversion and energy efficiency, as reported in many literatures [7,13,54]. Energy efficiency is increased by decreasing discharge power and increasing flow rate, whereas CO_2 conversion shows the opposite trend.

The effect of discharge power and CO_2 fraction and their interaction on energy efficiency at a flow rate of 110 ml/min for plasma with MgO/HKUST-1 catalyst is presented in Fig. 10 (b). Since effective conversion is used in energy efficiency, unlike CO_2 conversion, energy efficiency is decreased from a CO_2 fraction of 100%–50%, and it has a contrasting trend. The reason is part of the energy that Ar excitation and ionization consume. However, these species indirectly convert CO_2 ((R7), (R8)); a remarkable fraction of this energy is not used for CO_2 dissociation [32]. The maximum energy efficiency achieved at a discharge power of 50 W and a CO_2 fraction of 100%
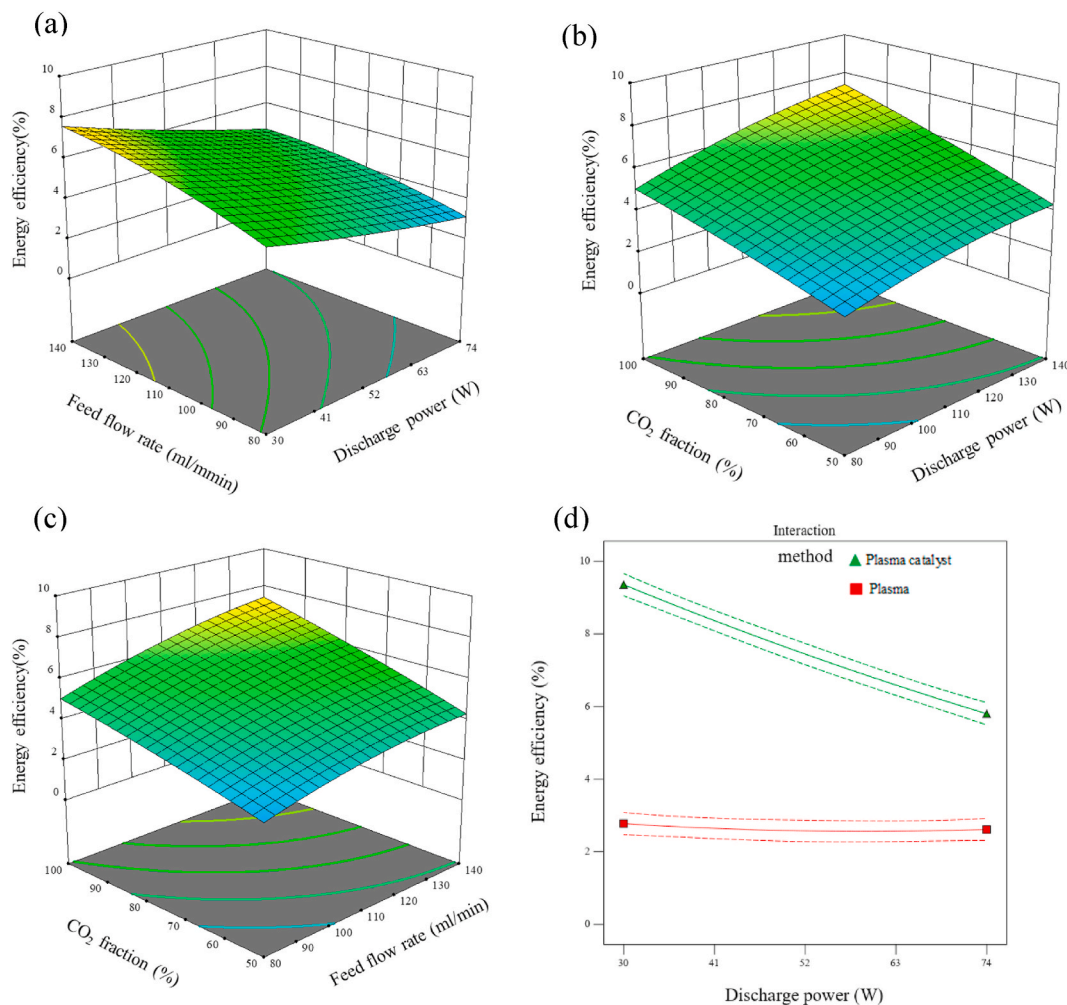
Fig. 10. Interaction between different plasma process parameters on the energy efficiency: (a) discharge power and feed flow rate; (b) discharge power and CO_2 fraction; (c) feed flow rate and CO_2 fraction; (d) discharge power and method.

was 8.2% in the plasma catalyst method, while the minimum was 3.1%. The plasma method's maximum was 3.2%, and the minimum was 2.1%. The p-value (0.0019) indicates that the interaction between these parameters is significant, and the F-value demonstrates that the CO_2 fraction (539.74) is more critical than the discharge power (407.32) in terms of energy efficiency.

The combined effects of the feed flow rate and CO_2 fraction at a discharge power of 52 W on the energy efficiency are depicted in Fig. 10 (c). At the minimum feed flow rate, the energy efficiency increases from 2.9% to 5.1% when the CO_2 fraction rises from 50% to 100 % in the plasm catalyst method (from 1.4% to 2.2% respectively in plasma without catalyst), while the energy efficiency increase over by 45% in plasma catalyst with a raise flow rate in CO_2 fraction 100%. As conducted in Table 6, the interaction between BC is significant (p-value <0.05).

Based on Table 6, among the different interactions, the AD has the highest F-value (230.77), which is more considerable in the energy efficiency as presented in Fig. 10 (d) at 140 ml/min feed flow rate and 100% CO_2 fraction, where the maximum energy efficiency reached at the discharge power 30 W (9.3% in plasma catalyst). In the plasma catalyst method, the energy efficiency is enhanced by 230% compared with the plasma method.

4. Conclusions

In this study, the effect of different process parameters (discharge power, feed flow rate, and CO_2 fraction) on CO_2 conversion, effective CO_2 conversion, and energy efficiency in a water-cooled DBD reactor without a catalyst and with MgO/HKUST-1 catalyst using CCD based RMS has been investigated. The ANOVA results confirmed that the regression models are significant and adequate for each response, and these results demonstrate that the effect of individual parameters is more important than the interaction between them.

Increasing the discharge power and decreasing the feed flow rate and CO_2 fraction, CO_2 conversion is increased. The highest CO_2

conversion and effective CO_2 conversion are 18.1% and 13.9%, respectively, in the presence of the catalyst, at maximum discharge power of 74 W and minimum feed flow rate of 80 ml/min, and CO_2 fraction. The discharge power is the most critical factor for both responses. Increasing the discharge power raises the number of micro-discharges and creates more energetic electrons and the reaction species, contributing to the conversion enhancement. As expected, there is a trade-off between CO_2 conversion and energy efficiency, so the maximum energy efficiency in the plasma without a catalyst and with a catalyst was 2.5% and 7.5%, which is achieved at the discharge power of 30 W, the feed flow rate of 140 ml/min, and CO_2 fraction of 75% (center point). At the lower CO_2 fraction, some of the energy in the plasma region is wasted, and the energy efficiency decreases. The method has the most significant effect on energy efficiency, followed by CO_2 fraction and discharge power.

CRediT authorship contribution statement

Hadi Hatami: Writing – original draft, Methodology, Investigation, Formal analysis, Data curation, Conceptualization. **Moham-madreza Khani:** Writing – review & editing, Visualization, Validation, Supervision, Project administration, Conceptualization. **Seyed Ali Razavi Rad:** Writing – review & editing, Software, Formal analysis. **Babak Shokri:** Writing – review & editing, Validation, Supervision, Conceptualization.

Declaration of competing interest

The authors declare that they have no known competing financial interests or personal relationships that could have appeared to influence the work reported in this paper.

References

[1] K.O. Yoro, M.O. Daramola, CO_2 emission sources, greenhouse gases, and the global warming effect, in: Adv. Carbon Capture Methods, Technol. Appl., Elsevier, 2020, pp. 3–28, https://doi.org/10.1016/B978-0-12-819657-1.00001-3.

[2] S.C. Peter, Reduction of CO_2 to chemicals and fuels: a solution to global warming and energy crisis, ACS Energy Lett. 3 (2018) 1557–1561, https://doi.org/10.1021/acsenergylett.8b00878.

[3] F. Golkar, S.M. Mousavi, Variation of XCO_2 anomaly patterns in the Middle East from OCO-2 satellite data, Int. J. Digit. Earth. 15 (2022) 1219–1235, https://doi.org/10.1080/17538947.2022.2096936.

[4] P. Ritchie, H, M. Roser, Rosado, CO_2 and Greenhouse Gas Emissions, Our World Data, 2020. https://ourworldindata.org/co2-emissions?utm_source=tri-citynews&utm_campaign=tricitynews%3Aoutbound&utm_medium=referral.

[5] P.R. Masson-Delmotte, V, P. Zhai, H.O. Pörtner, D. Roberts, J. Skea, Shukla, Global Warming of 1.5°C: IPCC Special Report on Impacts of Global Warming of 1.5°C above Pre-industrial Levels in Context of Strengthening Response to Climate Change, Sustainable Development, and Efforts to Eradicate Poverty, 2022. https://www.cambridge.org/core/books/global-warming-of-15c/D7455D42B4C820E706A03A169B1893FA%0A. https://www.ipcc.ch/site/assets/uploads/sites/2/2019/06/SR15_Full_Report_High_Res.pdf.

[6] R.M. Cuéllar-Franca, A. Azapagic, Carbon capture, storage and utilisation technologies: a critical analysis and comparison of their life cycle environmental impacts, J. CO_2 Util. 9 (2015) 82–102, https://doi.org/10.1016/j.jcou.2014.12.001.

[7] J. Li, S. Zhu, K. Lu, C. Ma, D. Yang, F. Yu, CO_2 conversion in a coaxial dielectric barrier discharge plasma reactor in the presence of mixed ZrO_2-CeO_2, J. Environ. Chem. Eng. 9 (2021), https://doi.org/10.1016/j.jece.2020.104654.

[8] Z. Farshidrokh, M.R. Khani, A. Khodadadi, M. Gharibi, B. Shokri, Dry reforming of methane over Ni/γ-MgO catalysts in a coaxial dielectric barrier discharge reactor, Chem. Eng. Technol. 44 (2021) 589–599, https://doi.org/10.1002/ceat.202000455.

[9] L. Wang, Y. Yi, H. Guo, X. Tu, Atmospheric pressure and room temperature synthesis of methanol through plasma-catalytic hydrogenation of CO_2, ACS Catal. 8 (2018) 90–100, https://doi.org/10.1021/acscatal.7b02733.

[10] Q. Zhang, S. Tao, J. Du, A. He, Y. Yang, C. Tao, A cold plasma-activated in situ AgCo surface alloy for enhancing the electroreduction of CO_2 to ethanol, J. Mater. Chem. A. 8 (2020) 8410–8420, https://doi.org/10.1039/D0TA01262A.

[11] Y. Wang, Y. Chen, J. Harding, H. He, A. Bogaerts, X. Tu, Catalyst-free single-step plasma reforming of CH_4 and CO_2 to higher value oxygenates under ambient conditions, Chem. Eng. J. 450 (2022) 137860, https://doi.org/10.1016/j.cej.2022.137860.

[12] K.R. Phillips, Y. Katayama, J. Hwang, Y. Shao-Horn, Sulfide-derived copper for electrochemical conversion of CO_2 to formic acid, J. Phys. Chem. Lett. 9 (2018) 4407–4412, https://doi.org/10.1021/acs.jpclett.8b01601.

[13] A. George, B. Shen, M. Craven, Y. Wang, D. Kang, C. Wu, X. Tu, A Review of Non-Thermal Plasma Technology: a novel solution for CO_2 conversion and utilization, Renew. Sustain. Energy Rev. 135 (2021), https://doi.org/10.1016/j.rser.2020.109702.

[14] X. Zhu, J.H. Liu, X.S. Li, J.L. Liu, X. Qu, A.M. Zhu, Enhanced effect of plasma on catalytic reduction of CO_2 to CO with hydrogen over Au/CeO_2 at low temperature, J. Energy Chem. 26 (2017) 488–493, https://doi.org/10.1016/j.jechem.2016.11.023.

[15] B. Ashford, Y. Wang, C.K. Poh, L. Chen, X. Tu, Plasma-catalytic conversion of CO_2 to CO over binary metal oxide catalysts at low temperatures, Appl. Catal. B Environ. 276 (2020), https://doi.org/10.1016/j.apcatb.2020.119110.

[16] R. Snoeckx, A. Bogaerts, Plasma technology – a novel solution for CO_2 conversion? Chem. Soc. Rev. 46 (2017) 5805–5863, https://doi.org/10.1039/C6CS00066E.

[17] S.-R. Lee, J. Lee, T. Lee, Y.F. Tsang, K.-H. Jeong, J.-I. Oh, E.E. Kwon, Strategic use of CO_2 for co-pyrolysis of swine manure and coal for energy recovery and waste disposal, J. CO_2 Util. 22 (2017) 110–116, https://doi.org/10.1016/j.jcou.2017.09.018.

[18] B. Wang, X. Wang, B. Zhang, Dielectric barrier micro-plasma reactor with segmented outer electrode for decomposition of pure CO_2, Front. Chem. Sci. Eng. 15 (2021) 687–697, https://doi.org/10.1007/s11705-020-1974-1.

[19] Y. Hua, J. Wang, T. Min, Z. Gao, Electrochemical CO_2 conversion towards syngas: recent catalysts and improving strategies for ratio-tunable syngas, J. Power Sources 535 (2022), https://doi.org/10.1016/j.jpowsour.2022.231453.

[20] A. Demont, S. Abanades, Solar thermochemical conversion of CO_2 into fuel via two-step redox cycling of non-stoichiometric Mn-containing perovskite oxides, J. Mater. Chem. A. 3 (2015) 3536–3546, https://doi.org/10.1039/c4ta06655c.

[21] P.R. Yaashikaa, P. Senthil Kumar, S.J. Varjani, A. Saravanan, A review on photochemical, biochemical and electrochemical transformation of CO_2 into value-added products, J. CO_2 Util. 33 (2019) 131–147, https://doi.org/10.1016/j.jcou.2019.05.017.

[22] R. Gupta, A. Mishra, Y. Thirupathaiah, A.K. Chandel, Biochemical Conversion of CO_2 in Fuels and Chemicals: Status, Innovation, and Industrial Aspects, Biomass Convers. Biorefinery, 2022, https://doi.org/10.1007/s13399-022-02552-8.

[23] D.P.H. Tran, M.T. Pham, X.T. Bui, Y.F. Wang, S.J. You, CeO_2 as a photocatalytic material for CO_2 conversion: a review, Sol. Energy 240 (2022) 443–466, https://doi.org/10.1016/j.solener.2022.04.051.

[24] B. Zhao, Y. Liu, Z. Zhu, H. Guo, X. Ma, Highly selective conversion of CO_2 into ethanol on $Cu/ZnO/Al_2O_3$ catalyst with the assistance of plasma, J. CO2 Util. 24 (2018) 34–39, https://doi.org/10.1016/j.jcou.2017.10.013.

[25] V. Ivanov, T. Paunska, S. Lazarova, A. Bogaerts, S. Kolev, Gliding arc/glow discharge for CO_2 conversion: comparing the performance of different discharge configurations, J. CO_2 Util. 67 (2023), https://doi.org/10.1016/j.jcou.2022.102300.

[26] M.Y. Ong, S. Nomanbhay, F. Kusumo, P.L. Show, Application of microwave plasma technology to convert carbon dioxide (CO_2) into high value products: a review, J. Clean. Prod. 336 (2022) 130447, https://doi.org/10.1016/j.jclepro.2022.130447.

[27] W. Ding, M. Xia, C. Shen, Y. Wang, Z. Zhang, X. Tu, C. Liu, Enhanced CO_2 conversion by frosted dielectric surface with ZrO_2 coating in a dielectric barrier discharge reactor, J. CO_2 Util. 61 (2022) 102045, https://doi.org/10.1016/j.jcou.2022.102045.

[28] E.C. Neyts, K. Ostrikov, M.K. Sunkara, A. Bogaerts, Plasma catalysis: synergistic effects at the nanoscale, Chem. Rev. 115 (2015) 13408–13446, https://doi.org/10.1021/acs.chemrev.5b00362.

[29] P. Wu, X. Li, N. Ullah, Z. Li, Synergistic effect of catalyst and plasma on CO_2 decomposition in a dielectric barrier discharge plasma reactor, Mol. Catal. 499 (2021), https://doi.org/10.1016/j.mcat.2020.111304.

[30] N. Lu, N. Liu, C. Zhang, Y. Su, K. Shang, N. Jiang, J. Li, Y. Wu, CO_2 conversion promoted by potassium intercaled $g-C_3N_4$ catalyst in DBD plasma system, Chem. Eng. J. 417 (2021), https://doi.org/10.1016/j.cej.2021.129283.

[31] N. Lu, C. Zhang, K. Shang, N. Jiang, J. Li, Y. Wu, Dielectric barrier discharge plasma assisted CO_2 conversion: understanding the effects of reactor design and operating parameters, J. Phys. D Appl. Phys. 52 (2019), https://doi.org/10.1088/1361-6463/ab0ebb.

[32] M. Ramakers, I. Michielsen, R. Aerts, V. Meynen, A. Bogaerts, Effect of argon or helium on the CO_2 conversion in a dielectric barrier discharge, Plasma Process. Polym. 12 (2015) 755–763, https://doi.org/10.1002/ppap.201400213.

[33] S. Xu, J.C. Whitehead, P.A. Martin, CO_2 conversion in a non-thermal, barium titanate packed bed plasma reactor: the effect of dilution by Ar and N_2, Chem. Eng. J. 327 (2017) 764–773, https://doi.org/10.1016/j.cej.2017.06.090.

[34] J.W. Maina, C. Pozo-Gonzalo, L. Kong, J. Schütz, M. Hill, L.F. Dumée, Metal organic framework based catalysts for CO_2 conversion, Mater. Horizons. 4 (2017) 345–361, https://doi.org/10.1039/c6mh00484a.

[35] W. Xu, M. Dong, L. Di, X. Zhang, A facile method for preparing uio-66 encapsulated ru catalyst and its application in plasma-assisted co_2 methanation, Nanomaterials 9 (2019), https://doi.org/10.3390/nano9101432.

[36] T.D. Hu, Y. Jiang, Y.H. Ding, Computational screening of metal-substituted HKUST-1 catalysts for chemical fixation of carbon dioxide into epoxides, J. Mater. Chem. A. 7 (2019) 14825–14834, https://doi.org/10.1039/c9ta02455g.

[37] P. Falcaro, R. Ricco, A. Yazdi, I. Imaz, S. Furukawa, D. Maspoch, R. Ameloot, J.D. Evans, C.J. Doonan, Application of metal and metal oxide nanoparticles at MOFs, Coord. Chem. Rev. 307 (2016) 237–254, https://doi.org/10.1016/j.ccr.2015.08.002.

[38] V. Hiremath, M.L.T. Trivino, J.G. Seo, Eutectic mixture promoted CO_2 sorption on $MgO-TiO_2$ composite at elevated temperature, J. Environ. Sci. (China) 76 (2019) 80–88, https://doi.org/10.1016/j.jes.2018.03.028.

[39] L. Wang, Y. Yao, T. Tran, P. Lira, S. Sternberg P.E, R. Davis, Z. Sun, Q. Lai, S. Toan, J. Luo, Y. Huang, Y.H. Hu, M. Fan, Mesoporous MgO enriched in Lewis base sites as effective catalysts for efficient CO_2 capture, J. Environ. Manag. 332 (2023), https://doi.org/10.1016/j.jenvman.2023.117398.

[40] M.A. Bezerra, R.E. Santelli, E.P. Oliveira, L.S. Villar, L.A. Escaleira, Response surface methodology (RSM) as a tool for optimization in analytical chemistry, Talanta 76 (2008) 965–977, https://doi.org/10.1016/j.talanta.2008.05.019.

[41] M. Hołub, On the measurement of plasma power in atmospheric pressure DBD plasma reactors, Int. J. Appl. Electromagn. Mech. 39 (2012) 81–87, https://doi.org/10.3233/JAE-2012-1446.

[42] T.C. Manley, The electric characteristics of the ozonator discharge, Trans. Electrochem. Soc. 84 (1943) 83, https://doi.org/10.1149/1.3071556.

[43] D. Ray, R. Saha, C. Subrahmanyam, DBD plasma assisted CO_2 decomposition: influence of diluent gases, Catalysts 7 (2017), https://doi.org/10.3390/catal7090244.

[44] D.C. Montgomery, Design and Analysis of Experiments, ninth ed., John wiley & sons, 2017.

[45] N. Bhoria, G. Basina, J. Pokhrel, K.S. Kumar Reddy, S. Anastasiou, V.V. Balasubramanian, Y.F. AlWahedi, G.N. Karanikolos, Functionalization effects on HKUST-1 and HKUST-1/graphene oxide hybrid adsorbents for hydrogen sulfide removal, J. Hazard Mater. 394 (2020), https://doi.org/10.1016/j.jhazmat.2020.122565.

[46] K.S. Lin, A.K. Adhikari, C.N. Ku, C.L. Chiang, H. Kuo, Synthesis and characterization of porous HKUST-1 metal organic frameworks for hydrogen storage, Int. J. Hydrogen Energy 37 (2012) 13865–13871, https://doi.org/10.1016/j.ijhydene.2012.04.105.

[47] Y. Zhong, Y. Chen, Y. Hu, G. Li, X. Xiao, Multifunctional MgO/HKUST-1 composite for capture, catalysis, and cyclic cataluminescence detection of esters all-in-one to rapidly identify scented products, Anal. Chem. 93 (2021) 16203–16212, https://doi.org/10.1021/acs.analchem.1c04100.

[48] H. Ghafuri, F. Ganjali, P. Hanifehnejad, Cu.BTC MOF as a novel and efficient catalyst for the synthesis of 1,8-Dioxo-octa-hydro xanthene, in: 24th Int. Electron. Conf. Synth, . Org. Chem., MDPI, Basel Switzerland, 2020, p. 2, https://doi.org/10.3390/ecsoc-24-08359.

[49] M.R. Bindhu, M. Umadevi, M. Kavin Micheal, M.V. Arasu, N. Abdullah Al-Dhabi, Structural, morphological and optical properties of MgO nanoparticles for antibacterial applications, Mater. Lett. 166 (2016) 19–22, https://doi.org/10.1016/j.matlet.2015.12.020.

[50] Y. Li, J. Zhao, D. Bu, X. Zhang, T. Peng, G. DI, X. Zhang, Plasma-assisted Co/Zr-metal organic framework catalysis of CO_2 hydrogenation: influence of Co precursors, Plasma Sci. Technol. 23 (2021) 055503, https://doi.org/10.1088/2058-6272/abeed9.

[51] R.A. Maia, B. Louis, W. Gao, Q. Wang, CO_2 adsorption mechanisms on MOFs: a case study of open metal sites, ultra-microporosity and flexible framework, React. Chem. Eng. 6 (2021) 1118–1133, https://doi.org/10.1039/D1RE00090J.

[52] G. Bang, K.-M. Kim, S. Jin, C.-H. Lee, Dynamic CO_2 sorption on MgO-based sorbent in the presence of CO and H_2O at elevated pressures, Chem. Eng. J. 433 (2022) 134607, https://doi.org/10.1016/j.cej.2022.134607.

[53] D. Mei, Y.L. He, S. Liu, J. Yan, X. Tu, Optimization of CO_2 conversion in a cylindrical dielectric barrier discharge reactor using design of experiments, Plasma Process. Polym. 13 (2016) 544–556, https://doi.org/10.1002/ppap.201500159.

[54] D.H. Mei, S.Y. Liu, X. Tu, CO_2 reforming with methane for syngas production using a dielectric barrier discharge plasma coupled with $Ni/\gamma-Al_2O_3$ catalysts: process optimization through response surface methodology, J. CO_2 Util. 21 (2017) 314–326, https://doi.org/10.1016/j.jcou.2017.06.020.

[55] A. Fridman, Plasma Chemistry, Cambridge University Press, 2008, https://doi.org/10.1017/CBO9780511546075.

[56] Y. Zeng, X. Tu, Plasma-catalytic hydrogenation of CO_2 for the cogeneration of CO and CH_4 in a dielectric barrier discharge reactor: effect of argon addition, J. Phys. D Appl. Phys. 50 (2017), https://doi.org/10.1088/1361-6463/aa64bb.